ACS APPLIED MATERIALS & INTERFACES

www.acsami.org

Research Article

Helicity-Resolved Vibrational Coupling in Twist WS_2/WSe_2 Heterostructures

Ke Wu, Wenyingdi He, Hongxia Zhong, Shutong Wu, Hongzhi Zhou, Shengjun Yuan,* Shunping Zhang,* and Hongxing Xu

Cite This: *ACS Appl. Mater. Interfaces* 2024, 16, 44186−44192

Read Online

ACCESS | Metrics & More | Article Recommendations | Supporting Information

ABSTRACT: Helicity-resolved Raman spectra can provide an intricate view into lattice structural details. Through the analysis of peak positions, intensities, and circular polarized Raman signals, a wealth of information about chiral structure arrangement within the moiré superlattice, interlayer interaction strength, polarizability change in chemical bond, and beyond can be unveiled. However, the relationship between the circular polarization of high-frequency Raman and twist angle is still not clear. Here, we utilize helicity-resolved Raman spectroscopy to explore the interlayer interactions and the effect of the moiré superlattice in WS_2/WSe_2 heterostructures. For the out-of-plane Raman mode A_{1g} of WS_2 (A_{1g} and $^1E_{2g}$ of WSe_2), its intensity is significantly enhanced (suppressed) in WS_2/WSe_2 heterostructures when θ is less than 10° or greater than 50°. This observation could be attributed to the large polarizability changes in both W−S and W−Se covalent bonds. The circular polarization of 2LA(M) in WSe_2 of the WS_2/WSe_2 heterostructure ($\theta < 10°$ or $\theta > 50°$) is significantly enhanced compared to that of 2LA(M) in the monolayer WSe_2. We deduce that the circular polarization of the Raman mode correlates with the proportion of high-symmetry area within a supercell of the moiré lattice. Our findings improve the understanding of twist-angle-modulated Raman modes in TMD heterostructures.

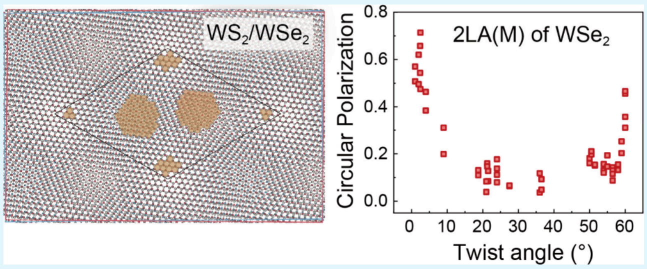

KEYWORDS: *moiré superlattice, WS_2/WSe_2, heterostructures, Raman, circular polarization, twist-angle*

1. INTRODUCTION

The moiré patterns formed in van der Waals heterostructures are of great interest in the study of semiconductor optoelectronic devices with valley or spin selection capabilities.[1−3] The period of the moiré pattern depends on the lattice constant mismatch and the stacking angle between the two layers of materials.[4−6] When the period of the moiré pattern is much larger than the individual lattice constant, people have given it a new name, called the moiré superlattice. The periodic potential field resulting from the periodic variations is termed the moiré potential. Especially, the moiré potential in transition metal dichalcogenide (TMD) heterostructures is predicted to have a depth greater than 100 meV.[2,7] Much efforts have been put in exploring the moiré superlattice engineered or moiré potential manipulated optical[1−3,8,9] and electronic properties.[9−13] For example, Van Hove singularities,[14] tunable insulating states,[10,15] and zero-resistances[13,16] states have been observed in twisted bilayer graphene. The interlayer excitons in heterostructures of TMDs exhibit alternative optical selection rules manipulated by the moiré superlattice.[3,17] What's more, moiré phonons, modulated by the moiré superlattice, have been observed in twisted MoS_2 bilayer.[18]

In twisted heterostructure, the interlayer coupling between the monolayers can lead to new peaks, energy shift, splitting etc., due to the breaking of the symmetry.[4,19−26] For example, the appearance of low-frequency shear modes or layer breathing modes are often related to the interlayer interactions.[27−31] The changes in those high-frequency optical phonon modes are associated with the variation in the overall lattice vibration characteristics.[4,27,28] Therefore, by investigating the variations of these Raman modes at different stacking angles, one can get a glimpse into the interlayer interactions and lattice properties of layered materials. Early study reveals that the out-of-plane modes of WSe_2 ($^1B_{2g}$, ∼309 cm^{-1}) and $MoSe_2$ ($^1B_{2g}$, ∼353 cm^{-1}) are sensitive to the interlayer coupling and can show up in all the twist angle $MoSe_2/WSe_2$ heterostructures.[4,32,33] The shear mode (layer breathing) is enhanced (disappeared) in $MoSe_2/WSe_2$ heterostructures with small twist angles (<5° or >55°). In the MoS_2/graphene heterostructure, the in-plane and out-of-plane Raman mode of MoS_2 can provide information about the in-plane strain and interfacial contact, respectively.[20] In the twisted MoS_2 bilayer,

Received: April 20, 2024
Revised: July 29, 2024
Accepted: July 29, 2024
Published: August 7, 2024

some folded optical and acoustic phonons were observed, which are also called moiré phonons, and their relationship with the twist angle was revealed.[18] Subsequently, several studies have reported the enhancement of Raman modes associated with interlayer coupling or novel moiré phonon phenomena.[34−38] By helicity-resolved Raman spectroscopy, it is revealed that the out-of-plane A_{1g} Raman mode of monolayer and multilayer TMDs maintains the same polarization with the excitation laser, while the in-plane $^1E_{2g}$ Raman mode exhibits the opposite polarization.[39,40] However, the evolution of Raman circular polarization in TMD heterostructures as a function of twist angle remains ambiguous.[19,21,33,35,41]

In this work, we carry nonpolarized and circular-polarized Raman characterization in WS_2/WSe_2 heterostructures and obtain the correlation between the Raman intensities, circular polarization, and the stacking angles. The intensity and position of the out-of-plane Raman mode of monolayers are more susceptible to interlayer coupling than that of the in-plane mode. The intensity of out-of-plane Raman mode for WS_2 and WSe_2 exhibit opposite variation with respect to the twist-angle. This can be attributed to the larger polarizability changes in both W−S and W−Se covalent bonds, resulting in significant variations in their intensities. Interestingly, the peak intensity of the second-order longitudinal acoustic (2LA) phonons of WSe_2 at M points of the Brillouin zone is also quenched in heterostructure for small twist angle and exhibits a variation pattern centered around 30°. Furthermore, the circular polarization of the 2LA(M) mode reaches its maximum in heterostructures with small twist-angles and exhibits a symmetric variation centered around 30°. We conclude that this variation in Raman circular polarization with stacking angle arises from the changes in the area of high-symmetry lattice domains within the moiré pattern, in which the different high-symmetry structures contribute to different circular-polarized Raman spectra. The room-temperature modulation of the moiré superlattice in circular-polarized Raman properties deepens our understanding of interlayer vibration coupling and provides new schemes for engineering electron−phonon coupling.[16,42−46]

2. RESULTS AND DISCUSSION

The WS_2/WSe_2 heterostructures were fabricated through dry mechanical transfer, and the twist angle was determined using polarization-resolved second harmonic characterization[47] (Figures S1−S3). Figure 1a shows an optical image of the WS_2/WSe_2 heterostructure with a 0° twist angle. All the Raman signals were excited by a continuous-wave 532 nm laser and dispersed by an 1800 lines/mm grating (see Methods). The nonpolarization resolved Raman spectra of the 0° WS_2/WSe_2 heterostructure are shown in Figure 1b. Some typical Raman modes can be identified and marked out by comparing with the Raman modes in the monolayer, including the in-plane ($^1E_{2g}$), out-of-plane (A_{1g}, $^1B_{2g}$, and 2LA(M) peak. In comparison to the monolayers, the 2LA(M) mode and A_{1g} and $^1E_{2g}$ modes (degenerate) of WSe_2 are significantly suppressed in the heterostructure, while the A_{1g} mode of WS_2 is enhanced in the heterostructure. To further resolve each peak, we used convoluted Lorentzian and Gaussian line shapes to fit the Raman spectra of the heterostructure, as shown in Figure 1c and 1d. The peak position of the $^1E_{2g}$(M), 2LA(M), $^1E_{2g}(\Gamma)$, and A_{1g} mode originated from WS_2 are found to 346.7 cm^{-1}, 352.6 cm^{-1}, 355.0 cm^{-1}, and 417.4 cm^{-1} on the heterostructure, in comparison with 345.2 cm^{-1}, 351.9 cm^{-1}, 356.7 cm^{-1}, and 417.2 cm^{-1} on monolayer WS_2.[48,49] The peak position of the $^1E_{2g}$ and A_{1g} and 2LA(M) mode of WSe_2 in heterostructure is 248.6 and 258.3 cm^{-1}, slightly different from 248.9 and 261.1 cm^{-1} on monolayer WSe_2.[4] Raman mode ($^1B_{2g}$) of multilayer WSe_2 materials shows up at 309 cm^{-1} in the heterostructures.

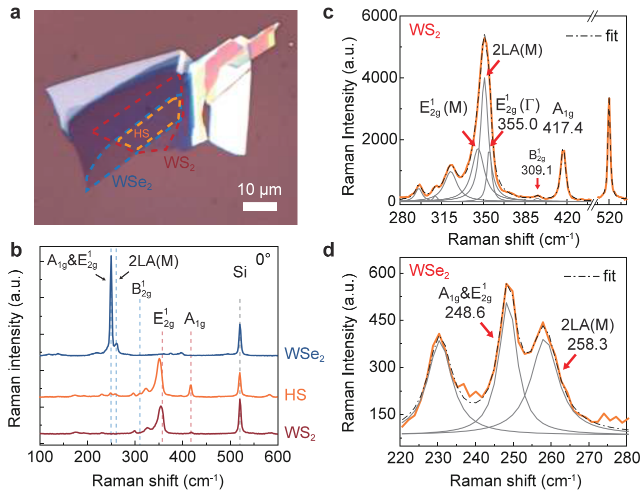

Figure 1. (a) Optical image of a WS_2/WSe_2 heterostructure (HS) with a 0° twist angle. The WS_2 monolayer, WSe_2 monolayer, and the heterostructure are outlined by red, blue, and orange dashed lines, respectively. Scale bar: 10 μm. (b) Raman spectra of the WS_2 monolayer, WSe_2 monolayer, and the WS_2/WSe_2 heterostructure with a 0° twist angle. Some typical Raman modes are indicated by dash lines. (c) and (d) show the fitting results of the Raman spectra from the heterostructure.

To investigate the influence of the moiré superlattice effect on Raman spectra, we conducted twist-angle-dependent Raman spectroscopic characterization on WS_2/WSe_2 heterostructures. Figure 2a shows the top view of WS_2/WSe_2 with different twist angles. Since both the hexagonal unit cell of WS_2 and WSe_2 layer are formed by covalent bonding of W atoms and S (Se) atoms, the WS_2 and WSe_2 lattices are aligned by 0°. The twist angle (θ) is defined as the angle between the lines connecting the upper layer W atoms and lower layer W atoms to the hexagonal center. The twist-angle-dependent Raman spectra are shown in Figure 2b. Obviously, the A_{1g} and $^1E_{2g}$ mode of WSe_2 and the A_{1g} mode of WS_2 exhibit pronounced intensity variations dependent on twist angle. Specifically, the intensity of the A_{1g} and $^1E_{2g}$ mode in WSe_2 exhibits a notable decrease in heterostructures at 0° or 60°, whereas the A_{1g} mode in WS_2 shows a noticeable enhancement under similar conditions. And the A_{1g} and $^1E_{2g}$ mode in WSe_2 is almost diminish in the 0° heterostructure. For out-of-plane Raman modes of WS_2 and WSe_2, the direction of atomic vibrations aligns with the direction of interlayer interactions. In the case of small-angle stacking (<10° or >50°), the enhanced interlayer coupling increases the change in polarizability of both W−S and W−Se bonds, leading to a significant change in their intensities. A novel Raman mode at approximately 309 cm^{-1} emerges consistently across all the WS_2/WSe_2 heterostructure, which is attributed to an out-of-plane Raman mode ($^1B_{2g}$) in multilayer WSe_2 materials.[4] This observation strongly suggests robust interlayer coupling within our samples. According to our statistics, the moiré superlattice influences the intensity, peak position, and line width of the high-

https://doi.org/10.1021/acsami.4c06488
ACS Appl. Mater. Interfaces 2024, 16, 44186−44192

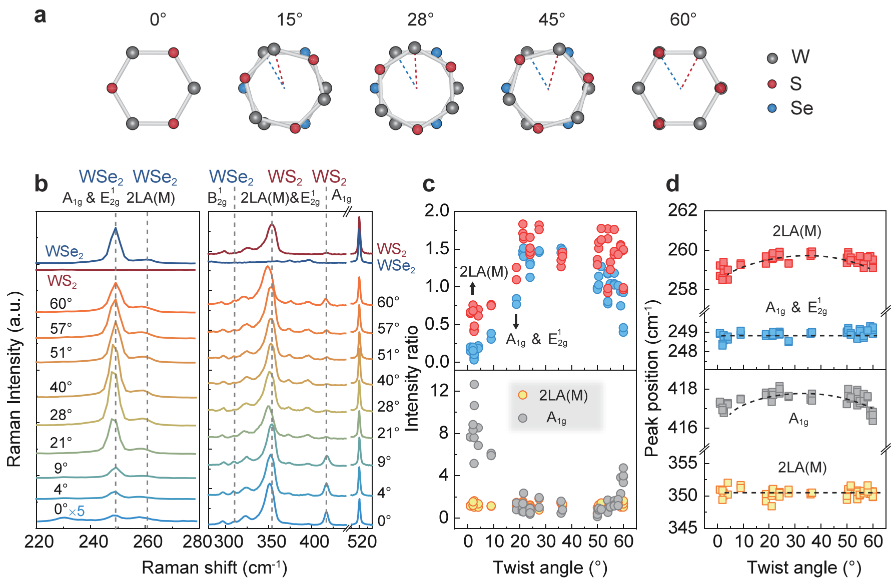

Figure 2. (a) Top view of WS_2/WSe_2 heterostructure with various twist angles (0°, 15°, 28°, 45°, and 60°). The red and blue dotted lines connect the centers to the W atom of WS_2 (Top) and WSe_2 (bottom) layer, respectively. And the angle between the two lines is defined as the twist angle. (b) The twist-angle-dependent Raman spectra of the WS_2/WSe_2 heterostructure. The dashed lines label the Raman modes investigated. The Raman spectra taken from the WSe_2 (blue) and WS_2 (red) monolayers are also included for comparison. For clarity, the curves are vertically shifted and their order are intentionally altered to avoid overlap. (c) The relationship between the Raman enhancement ratio and the stacking angle. The ratio is defined as the peak intensity on the heterostructure to the peak intensity of the corresponding monolayer. (d) The twist-angle-dependent Raman peak positions. The black dash lines are plotted for eye guidance.

frequency Raman modes. Figure 2c shows the twist-angle-dependent Raman enhanced ratio, which is defined as the Raman intensity in the heterostructure to that in the corresponding monolayer. Both the A_{1g} and $^1E_{2g}$ and 2LA(M) mode of WSe_2 is suppressed in heterostructures with small twist angles (<10° or >50°). However, the out-of-plane A_{1g} mode of WS_2 is significantly enhanced in heterostructures with small twist angles. The Raman intensity of 2LA(M) and $^1E_{2g}(\Gamma)$ phonon modes of WS_2 do not exhibit a modulation pattern influenced by the twist-angles, as shown in Figure 2c and Figure S4c. For the $^1E_{2g}$(M) of WS_2 at 345 cm^{-1}, its intensity is enhanced as the twist angle approaches 0° or 60° (Figure S4c). The twist-angle-dependent peak positions are depicted in Figure 2d and Figure S4b. The 2LA(M) mode of WSe_2 and the A_{1g} mode of WS_2 exhibit variations dependent on the twist-angle. As the twist angle approaches 0° or 60°, these peaks shift to lower Raman frequencies introduced by the decreased interlayer distance. In contrast, the peak position of the A_{1g} and $^1E_{2g}$ modes of WSe_2, as well as the 2LA(M) of WS_2, do not exhibit twist-angle modulated patterns. The analysis of the line width of A_{1g} of WS_2, A_{1g} and $^1E_{2g}$, and 2LA(M) of WSe_2 with respect to the stacking angle are also presented in Figure S4. As the angle approaches 0° or 60°, the line widths of these peaks gradually increase in a twist-angle-sensitive manner. The broadening of peak widths may be attributed to enhanced interlayer coupling, which increases electron−phonon interactions and consequently enhances phonon scattering, leading to the broadening of the peaks sensitive to twist angles. Interestingly, the line width of $^1E_{2g}$(M), 2LA(M), and $^1E_{2g}(\Gamma)$ of WS_2 decreased as the stacking angle approached 0° or 60°. More analyses of Raman modes at around 309 cm^{-1}, 320 cm^{-1}, and 395 cm^{-1} are shown in Figure S5. Above all, the out-of-plane Raman mode is more susceptible to interlayer coupling compared to in-plane modes in positions, peaks, and intensities. Similar phonon modes of this kind are commonly observed in low-frequency Raman spectra.[18,50] Note that these Raman properties are independent of both the stacking order of WS_2 and WSe_2 and the linear polarization of the excitation. Figure S6 shows the Raman spectra dependent on the twist angle of the WSe_2/WS_2 (WSe_2 on top of the WS_2) heterostructure. The Raman spectra excited under horizontal and vertical linear polarization are shown in Figure S7.

To delve deeper into the Raman properties modulated by the moiré superlattice, we performed helicity-resolved Raman characterization of these heterostructures. Figure 3a depicts helicity-resolved Raman spectra of a 2° heterostructure excited by a right circularly polarized (σ^+) 532 nm continuous laser and collected with σ^+ or σ^- signals. The circular-polarized Raman spectra of monolayer MoS_2, WS_2, and WSe_2 can be found in Figure S9, which shows that different Raman modes have different degrees of circular polarization $CP = \frac{I(\sigma^+) - I(\sigma^-)}{I(\sigma^+) + I(\sigma^-)}$, where I (σ^+) and I (σ^-) are the right-handed or left-handed Raman intensity. Figure 3b presents the twist-angle-dependent circularly polarized A_{1g} and $^1E_{2g}$ and 2LA(M) modes of WSe_2 and the A_{1g} mode of WS_2, which is obviously twist-angle-dependent in nonpolarized Raman characterization. The CP statistics for these Raman modes are displayed in Figure 3c. Differing from the significant changes in Raman peak intensity and position, the CP values of both the A_{1g} and $^1E_{2g}$ mode of WSe_2 and the A_{1g} mode of WS_2 in the heterostructures remain relatively stable at around 0.76 and 1.0. These values closely resemble their corresponding CP values in monolayers WSe_2 (0.66) and WS_2 (1.0) (Figure S9). Neither of them exhibit moiré superlattice modulated symmetry patterns, except for a reduction when the twist angle is close to 0°. This circular polarization value aligns with the selection rules dictated by their Raman tensors.[39,40] For the A_{1g} mode in multilayer or the A′ 1 mode in monolayer TMDs, the Raman tensor (R) is

https://doi.org/10.1021/acsami.4c06488
ACS Appl. Mater. Interfaces 2024, 16, 44186−44192

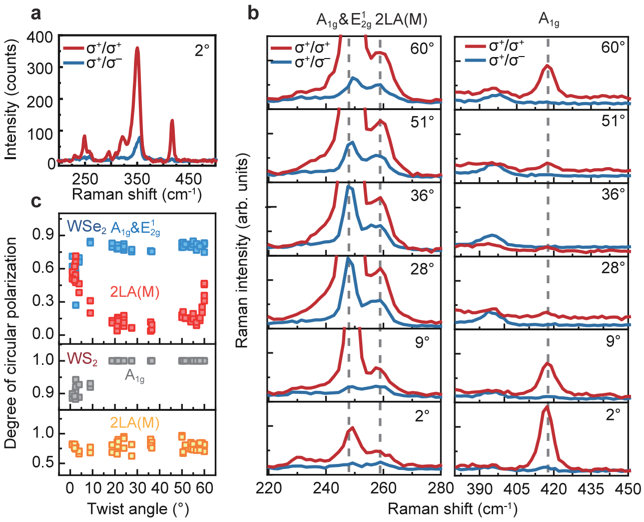

Figure 3. (a) Circularly polarized Raman spectra of a 2° WS_2/WSe_2 heterostructure under a σ^+ polarized laser at 532 nm. (b) The circular polarized Raman spectra with various twist angles. The left panel displays the A_{1g} and $^1E_{2g}$ and 2LA(M) Raman modes of the WSe_2 layer in WS_2/WSe_2 heterostructures. The right panel shows the A_{1g} Raman mode of the WS_2 layer in the heterostructures. (c) The twist-angle-dependent circular polarization of select Raman modes of the heterostructures.

$$\begin{bmatrix} a & 0 & 0 \\ 0 & a & 0 \\ 0 & 0 & b \end{bmatrix}$$

. For the σ^+/σ^+ configuration, both the excitation (σ_e) and detection (σ_d) are right-handed circular polarization $\sigma_e = \sigma_d = \frac{1}{\sqrt{2}}\begin{pmatrix} 1 \\ 0 \end{pmatrix} \text{i}$, $\sigma_e^* R \sigma_d = a$. For the opposite σ^+/σ^- configuration, $\sigma_e = \frac{1}{\sqrt{2}}\begin{pmatrix} 1 \\ 0 \end{pmatrix} i$ and $\sigma_d = \frac{1}{\sqrt{2}}\begin{pmatrix} 1 \\ i \\ 0 \end{pmatrix}$, $\sigma_e^* R \sigma_d = 0$. Thereby, the CP values of A_{1g} of WS_2 remain around 1 in both monolayers and heterostructures. For the E_{2g} (multilayer)/E′ (monolayer), the $\sigma_e^* R \sigma_d$ is zero (nonzero) for the σ^+/σ^+ (σ^+/σ^-) settings. For the A_{1g} and $^1E_{2g}$ mode of WSe_2, its CP values in both monolayer and heterostructure are slightly less than 1, which could stem from the partial degeneracy of the A_{1g} and $^1E_{2g}$ modes, resulting in a CP value slightly below 1. The CP of the 2LA(M) modes of WS_2 also consistently remain at approximately 0.78 in all the heterostructures with various twist-angle, which is slightly smaller than the CP value of 0.86 observed in the corresponding monolayer WS_2. However, it is worth noting that the CP of the second order 2LA(M) mode of WSe_2 exhibits a symmetry variation centered around 30°. It is significantly enhanced in the WS_2/WSe_2 heterostructures near 0° or 60° and decreased as the twist angle gets close to 30°, while the CP of the 2LA(M) mode in monolayer WSe_2 is nearly zero (Figure S9). The twist-angle-modulated CP value of Raman mode was not found to be not related to the valley-selective properties of monolayer excitons and interlayer excitons. Further discussions can be found in Figure S10.

In principle, the CP of A_{1g} and E_{2g} in monolayer and bilayer TMDs should exhibit a similar behavior, owing to their shared Raman tensors. In the heterostructure moiré superlattice, these Raman modes should maintain consistent CP though there might be some overall shifts in the magnitude due to the varying strength of interlayer coupling or the changed bond length between the heterostructure. For example, in our experiments, the CP of both the A_{1g} and $^1E_{2g}$ mode of WSe_2, as well as the A_{1g} modes of WS_2, are close to the corresponding CP values of monolayers (Figure S9). And the slight decrease in CP observed in nearly 0° heterostructures can be attributed to the enhanced out-of-plane vibration resulting from the enlarged AA stacking area in nearly 0° heterostructure. Similar decreased circular polarization of the A_{1g} mode of WS_2 has also been observed in $WS_2/MoSe_2$ heterostructures (Figure S11). However, concerning the 2LA(M) mode of WSe_2 in the heterostructure, its CP value remains around 0.15 in WS_2/WSe_2 heterostructures with $10° < \theta < 50°$, which is close to its value (0.16) in monolayer WSe_2. We attribute this to the weak interlayer coupling, which causes the heterostructure to manifest monolayer properties. Subsequently, the CP value increases to around 0.6 as the twist angle varies from 10° to 0° or 50° to 60°. We attribute this increased CP of the 2LA(M) mode to the increased area of the high-symmetry lattice structure in the heterostructure. Figure 4a depicts the side view

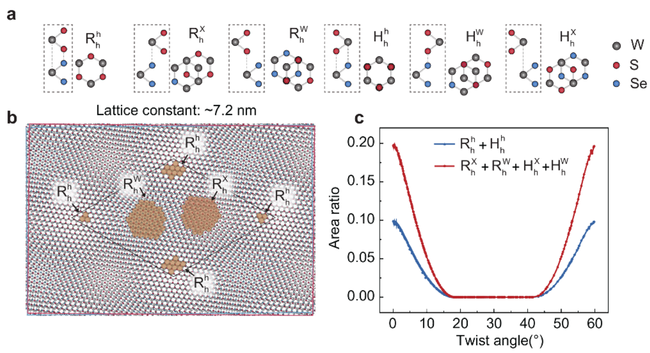

Figure 4. (a) Side view (left) and top view (right) of the high symmetry sites in the moiré superlattice. (b) The moiré superlattice formed in a 1° WS_2/WSe_2 heterostructures with high-symmetry sites marked by the brown shade. (c) The area ratio as a function of twist angle. The ratio is obtained by dividing the high-symmetry area by the area of unit cell in the moiré superlattice, as indicated by the rhombus in (b).

(dotted rectangle) and top view of the high symmetry structure in moiré superlattice, $R^{h\,h}$ ($H^{h\,h}$) refers to R-type (H-type), where the hexagon center (h) of WS_2 layer aligns the hexagon center (h) of WSe_2 layer. And $R^{X\,h}$ and $R^{W\,h}$ can be comprehended in the same way, where the *W* stands for a *W* atom and *X* stands for S or Se atoms. Figure 4b illustrates a typical moiré superlattice in a WS_2/WSe_2 heterostructure with a 1° twist-angle, while the specific sites depicted in Figure 4a are shaded in a brown color. We constructed the unrelaxed periodic unit cell in WS_2/WSe_2 heterostructure under a certain twist angle and calculated the area of all the specific sites. The lattice constant of WS_2 (WSe_2) is 3.181 Å (3.315 Å). The periodic structure was constructed by hexagons in the WSe_2 layer. A hexagon is aligned by straight lines connecting centers of each atom in WSe_2 layer, and a hexagon can be counted as high-symmetry area, for example, $R^{h\,h}$ structure, as long as it satisfies that all six atoms on the vertex deviate no more than 0.6 Å on the two-dimensional plane from the corresponding atoms in the other layer. Other high-symmetry area can also be calculated based on this method. According to previous calculated chiral phonon modes of twisted bilayer WSe_2, the chirality of both flat acoustic and optical phonon is enhanced

https://doi.org/10.1021/acsami.4c06488
ACS Appl. Mater. Interfaces 2024, 16, 44186−44192

when the twist angle increases from 50° to 60°.[34] And the calculations also unveil that the different lattice structures in the moiré lattice contribute different chirality.[36] Therefore, we attribute the twist-angle-dependent behaviors of the CP value of the 2LA(M) mode of WSe_2 in the WS_2/WSe_2 heterostructures to the variation in the area of the high-symmetry lattice structures as the twist angle changes. The correlation between the fraction of high-symmetry lattice area in the moiré superlattice and twist angle is illustrated in Figure 4c, following a pattern centered around 30°. The correspondence between the calculation and experiment is qualitative. More calculations are required to conclude quantitative results, for example, which symmetrical sites contribute to σ^+ or σ^- Raman vibration mode and the second order Raman transition process in a moiré superlattice, and so on.

3. CONCLUSION

In conclusion, we explored the twist-angle-dependent Raman spectra of WS_2/WSe_2 heterostructures. The A_{1g} modes are more susceptible to variation of twist-angle. In the non-polarized Raman characterization, both the intensity and position of the out-of-plane Raman mode of WSe_2 and WS_2 exhibit an obviously twist-angle-dependent pattern. Their intensity dependence on with the twist-angles is opposite. For the out-of-plane Raman mode A_{1g} of WS_2 (A_{1g} and $^1E_{2g}$ of WSe_2), its intensity becomes stronger (weaker) when $\theta < 10°$ or $\theta > 50°$. We attribute the large amplitude changes in the out-of-plane mode of WS_2 and WSe_2 in the heterostructures to significant variations in the polarizability of W−S and W−Se chemical bonds in the aligned or antialigned heterostructures. Interestingly, in the circular-polarized Raman characterization, the CP of 2LA(M) mode of WSe_2 in the heterostructures also exhibits a twist-angle-dependent pattern. We speculate that the dependence of CP on the twist angle is positively correlated with the area ratio of high-symmetry lattice sites in the moiré superlattice. These results can deepen the understanding of interlayer interaction in TMD heterostructures, and the effect of moiré superlattice on the pristine Raman modes in the original lattice.

4. METHODS

Sample Preparation. All of the heterostructures were fabricated using a standard dry transfer method under a microscope. The polymer used in the transfer process is PVA (poly(vinyl alcohol)). Then the heterostructures were annealed at 300 °C for 3 h. More details about the stacking can be found in reference.[47]

Raman Characterization. Both the nonpolarized and circular-polarized Raman spectra were excited using a 532 nm continuous laser. The signals were collected through a 100× objective (NA = 0.9), dispersed by a 1800 lines/mm grating, and analyzed using a Raman spectrometer (Renishaw inVia). A quarter-wave plate of 532 nm is placed in front of the microscope. More details about the optical setup can be found in Figure S8.

■ ASSOCIATED CONTENT

Supporting Information

The Supporting Information is available free of charge at https://pubs.acs.org/doi/10.1021/acsami.4c06488.

Polar plot SHG intensity for WS_2/WSe_2; twist-angle-dependent Raman shift, intensity ratio, and line width of $^1E_{2g}$(M), 2LA(M), $^1E_{2g}(\Gamma)$ of WS_2, 309 cm^{-1} ($^1B_{2g}$ of WSe_2), 320 cm^{-1} (WS_2), and 395 cm^{-1} (WSe_2) in WS_2/WSe_2 heterostructures; twist-angle-dependent Raman spectra of the WSe_2/WS_2 heterostructures (top: WSe_2, bottom:WS_2); twist-angle-modulated Raman peaks and intensities of WS_2/WSe_2 excited under horizontal linear polarization and vertical linear polarization; optical path diagram; helicity-resolved Raman spectra of monolayer TMDs and $WS_2/MoSe_2$ heterostructures; helicity-resolved PL spectra of monolayer WS_2, WSe_2, and WS_2/WSe_2 heterostructures (PDF)

■ AUTHOR INFORMATION

Corresponding Authors

Shengjun Yuan − *School of Physics and Technology and Key Laboratory of Artificial Micro- and Nano-structures of Ministry of Education, Wuhan University, Wuhan 430072, China; Wuhan Institute of Quantum Technology, Wuhan 430206, China;* orcid.org/0000-0001-6208-1502; Email: spzhang@whu.edu.cn

Shunping Zhang − *School of Physics and Technology and Key Laboratory of Artificial Micro- and Nano-structures of Ministry of Education, Wuhan University, Wuhan 430072, China; Wuhan Institute of Quantum Technology, Wuhan 430206, China;* orcid.org/0000-0002-8491-0903; Email: s.yuan@whu.edu.cn

Authors

Ke Wu − *School of Physics and Technology and Key Laboratory of Artificial Micro- and Nano-structures of Ministry of Education, Wuhan University, Wuhan 430072, China; School of Sciences, Hangzhou Dianzi University, Hangzhou 310018, China;* orcid.org/0009-0002-2701-494X

Wenyingdi He − *School of Physics and Technology and Key Laboratory of Artificial Micro- and Nano-structures of Ministry of Education, Wuhan University, Wuhan 430072, China*

Hongxia Zhong − *School of Mathematics and Physics, China University of Geosciences, Wuhan 430074, China*

Shutong Wu − *School of Sciences, Hangzhou Dianzi University, Hangzhou 310018, China*

Hongzhi Zhou − *ZJU-Hangzhou Global Scientific and Technological Innovation Center, Hangzhou, Zhejiang 311200, China;* orcid.org/0000-0001-6947-9265

Hongxing Xu − *School of Physics and Technology and Key Laboratory of Artificial Micro- and Nano-structures of Ministry of Education, Wuhan University, Wuhan 430072, China; School of Microelectronics, Wuhan University, Wuhan 430072, China; Institute of Quantum Materials and Physics, Henan Academy of Sciences, Zhengzhou 450046, China;* orcid.org/0000-0002-1718-8834

Complete contact information is available at: https://pubs.acs.org/10.1021/acsami.4c06488

Notes

The authors declare no competing financial interest.

■ ACKNOWLEDGMENTS

This work was supported by the National Natural Science Foundation of China (Grant 12134011). Zhejiang Provincial Natural Science Foundation of China (Grant No. LQ23A040011), Fundamental Research Funds for the Provincial Universities of Zhejiang (Grant GK239909299001-401), The National Natural Science

Foundation of China (Grant 12104421 and 11947218), and Zhejiang Provincial Natural Science Foundation of China (Grant No. LY23A040005). H.Z. thanks the China Postdoctoral Science Foundation (Grant No. 2022M722727) for the financial support. We thank the Center for Nanoscience and Nanotechnology at Wuhan University for the support. K.W. gratefully acknowledges Prof. Haiming Zhu's group at Zhejiang University for the help with polarized-resolved second-harmonic measurements. K.W. gratefully acknowledges Prof. Liang Hu's group at Hangzhou Dianzi University for the help with sample preparation.

REFERENCES

(1) Jin, C.; Regan, E. C.; Yan, A.; Iqbal Bakti Utama, M.; Wang, D.; Zhao, S.; Qin, Y.; Yang, S.; Zheng, Z.; Shi, S.; Watanabe, K.; Taniguchi, T.; Tongay, S.; Zettl, A.; Wang, F. Observation of moiré excitons in WSe_2/WS_2 heterostructure superlattices. *Nature* **2019**, *567*, 76−80.

(2) Seyler, K. L.; Rivera, P.; Yu, H. Y.; Wilson, N. P.; Ray, E. L.; Mandrus, D. G.; Yan, J. Q.; Yao, W.; Xu, X. D. Signatures of moiré-trapped valley excitons in $MoSe_2/WSe_2$ heterobilayers. *Nature* **2019**, *567*, 66−70.

(3) Tran, K.; Moody, G.; Wu, F.; Lu, X.; Choi, J.; Kim, K.; Rai, A.; Sanchez, D. A.; Quan, J.; Singh, A.; Embley, J.; Zepeda, A.; Campbell, M.; Autry, T.; Taniguchi, T.; Watanabe, K.; Lu, N.; Banerjee, S. K.; Silverman, K. L.; Kim, S.; Tutuc, E.; Yang, L.; MacDonald, A. H.; Li, X. Evidence for moiré excitons in van der Waals heterostructures. *Nature* **2019**, *567*, 71−75.

(4) Nayak, P. K.; Horbatenko, Y.; Ahn, S.; Kim, G.; Lee, J. U.; Ma, K. Y.; Jang, A. R.; Lim, H.; Kim, D.; Ryu, S.; Cheong, H.; Park, N.; Shin, H. S. Probing evolution of twist-angle-dependent interlayer excitons in $MoSe_2/WSe_2$ van der Waals heterostructures. *ACS Nano* **2017**, *11*, 4041−4050.

(5) Alexeev, E. M.; Ruiz-Tijerina, D. A.; Danovich, M.; Hamer, M. J.; Terry, D. J.; Nayak, P. K.; Ahn, S.; Pak, S.; Lee, J.; Sohn, J. I.; Molas, M. R.; Koperski, M.; Watanabe, K.; Taniguchi, T.; Novoselov, K. S.; Gorbachev, R. V.; Shin, H. S.; Fal'ko, V. I.; Tartakovskii, A. I. Resonantly hybridized excitons in moiré superlattices in van der Waals heterostructures. *Nature* **2019**, *567*, 81−86.

(6) Liao, M. Z.; Wei, Z.; Du, L. J.; Wang, Q. Q.; Tang, J.; Yu, H.; Wu, F. F.; Zhao, J. J.; Xu, X. Z.; Han, B.; et al. Precise control of the interlayer twist angle in large scale MoS_2 homostructures. *Nat. Commun.* **2020**, *11*, 2153.

(7) Yu, H.; Liu, G.; Tang, J.; Xu, X.; Yao, W. Moiré excitons: From programmable quantum emitter arrays to spin-orbit-coupled artificial lattices. *Sci. Adv.* **2017**, *3*, No. e1701696.

(8) Baek, H.; Brotons-Gisbert, M.; Koong, Z. X.; Campbell, A.; Rambach, M.; Watanabe, K.; Taniguchi, T.; Gerardot, B. D. Highly energy-tunable quantum light from moiré-trapped excitons. *Sci. Adv.* **2020**, *6*, No. eaba8526.

(9) Chen, D.; Lian, Z.; Huang, X.; Su, Y.; Rashetnia, M.; Yan, L.; Blei, M.; Taniguchi, T.; Watanabe, K.; Tongay, S.; et al. Tuning moiré excitons and correlated electronic states through layer degree of freedom. *Nat. Commun.* **2022**, *13*, 4810.

(10) Cao, Y.; Fatemi, V.; Demir, A.; Fang, S.; Tomarken, S. L.; Luo, J. Y.; Sanchez-Yamagishi, J. D.; Watanabe, K.; Taniguchi, T.; Kaxiras, E.; Ashoori, R. C.; Jarillo-Herrero, P. Correlated insulator behaviour at half-filling in magic-angle graphene superlattices. *Nature* **2018**, *556*, 80−84.

(11) Bistritzer, R.; MacDonald, A. H. Moiré bands in twisted double-layer graphene. *Proc. Natl. Acad. Sci. U.S.A.* **2011**, *108*, 12233−12237.

(12) Sharpe, A. L.; Fox, E. J.; Barnard, A. W.; Finney, J.; Watanabe, K.; Taniguchi, T.; Kastner, M. A.; Goldhaber-Gordon, D. Emergent ferromagnetism near three-quarters filling in twisted bilayer graphene. *Science* **2019**, *365*, 605−608.

(13) Cao, Y.; Fatemi, V.; Fang, S.; Watanabe, K.; Taniguchi, T.; Kaxiras, E.; Jarillo-Herrero, P. Unconventional superconductivity in magic-angle graphene superlattices. *Nature* **2018**, *556*, 43−50.

(14) Li, G.; Luican, A.; Lopes dos Santos, J. M. B.; Castro Neto, A. H.; Reina, A.; Kong, J.; Andrei, E. Y. Observation of Van Hove singularities in twisted graphene layers. *Nat. Phys.* **2010**, *6*, 109−113.

(15) Chen, G. R.; Jiang, L. L.; Wu, S.; Lyu, B.; Li, H. Y.; Chittari, B. L.; Watanabe, K.; Taniguchi, T.; Shi, Z. W.; Jung, J.; Zhang, Y. B.; Wang, F. Evidence of a gate-tunable Mott insulator in a trilayer graphene moiré superlattice. *Nat. Phys.* **2019**, *15*, 237−241.

(16) Shavit, G.; Berg, E.; Stern, A.; Oreg, Y. Theory of correlated insulators and superconductivity in twisted bilayer graphene. *Phys. Rev. Lett.* **2021**, *127*, 247703.

(17) Tartakovskii, A. Excitons in 2D heterostructures. *Nature Reviews Physics* **2020**, *2*, 8−9.

(18) Lin, M. L.; Tan, Q. H.; Wu, J. B.; Chen, X. S.; Wang, J. H.; Pan, Y. H.; Zhang, X.; Cong, X.; Zhang, J.; Ji, W.; Hu, P. A.; Liu, K. H.; Tan, P. H. Moiré phonons in twisted bilayer MoS_2. *ACS Nano* **2018**, *12*, 8770−8780.

(19) Chuang, H. J.; Phillips, M.; McCreary, K. M.; Wickramaratne, D.; Rosenberger, M. R.; Oleshko, V. P.; Proscia, N. V.; Lohmann, M.; O'Hara, D. J.; Cunningham, P. D.; Hellberg, C. S.; Jonker, B. T. Emergent moiré phonons due to zone folding in WSe_2-WS_2 van der Waals heterostructures. *ACS Nano* **2022**, *16*, 16260−16270.

(20) Li, H.; Wu, J. B.; Ran, F. R.; Lin, M. L.; Liu, X. L.; Zhao, Y. Y.; Lu, X.; Xiong, Q. H.; Zhang, J.; Huang, W.; Zhang, H.; Tan, P. H. Interfacial interactions in van der Waals heterostructures of MoS_2 and graphene. *ACS Nano* **2017**, *11*, 11714−11723.

(21) Wang, D.; Zhang, Z. W.; Huang, B. L.; Zhang, H. M.; Huang, Z. W.; Liu, M. M.; Duan, X. D. Few-layer WS_2-WSe_2 lateral heterostructures: influence of the gas precursor selenium/tungsten ratio on the number of layers. *ACS Nano* **2022**, *16*, 1198−1207.

(22) van der Zande, A. M.; Kunstmann, J.; Chernikov, A.; Chenet, D. A.; You, Y.; Zhang, X.; Huang, P. Y.; Berkelbach, T. C.; Wang, L.; Zhang, F.; et al. Tailoring the electronic structure in bilayer molybdenum disulfide via interlayer twist. *Nano Lett.* **2014**, *14*, 3869−3875.

(23) Carozo, V.; Almeida, C. M.; Ferreira, E. H. M.; Cançado, L. G.; Achete, C. A.; Jorio, A. Raman signature of graphene superlattices. *Nano Lett.* **2011**, *11*, 4527−4534.

(24) Popov, V. N. Raman bands of twisted bilayer graphene. *J. Raman Spectrosc.* **2018**, *49*, 31−35.

(25) Eckmann, A.; Park, J.; Yang, H. F.; Elias, D.; Mayorov, A. S.; Yu, G. L.; Jalil, R.; Novoselov, K. S.; Gorbachev, R. V.; Lazzeri, M.; Geim, A. K.; Casiraghi, C. Raman fingerprint of aligned graphene/h-BN superlattices. *Nano Lett.* **2013**, *13*, 5242−5246.

(26) Wu, J. B.; Zhang, X.; Ijäs, M.; Han, W. P.; Qiao, X. F.; Li, X. L.; Jiang, D. S.; Ferrari, A. C.; Tan, P. H. Resonant raman spectroscopy of twisted multilayer graphene. *Nat. Commun.* **2014**, *5*, 5309.

(27) Li, Z. Y.; Lai, J. M.; Zhang, J. Review of phonons in moiré superlattices. *J. Semicond.* **2023**, *44*, 011902.

(28) Cong, X.; Lin, M. L.; Tan, P. H. Lattice vibration and raman scattering of two-dimensional van der Waals heterostructure. *J. Semicond.* **2019**, *40*, 091001.

(29) Huang, S. X.; Liang, L. B.; Ling, X.; Puretzky, A. A.; Geohegan, D. B.; Sumpter, B. G.; Kong, J.; Meunier, V.; Dresselhaus, M. S. Low-frequency interlayer raman modes to probe interface of twisted bilayer MoS_2. *Nano Lett.* **2016**, *16*, 1435−1444.

(30) Liang, L. B.; Zhang, J.; Sumpter, B. G.; Tan, Q. H.; Tan, P. H.; Meunier, V. Low-frequency shear and layer-breathing modes in raman scattering of two-dimensional materials. *ACS Nano* **2017**, *11*, 11777−11802.

(31) Lu, X.; Utama, M. I. B.; Lin, J. H.; Luo, X.; Zhao, Y. Y.; Zhang, J.; Pantelides, S. T.; Zhou, W.; Quek, S. Y.; Xiong, Q. H. Rapid and Nondestructive Identification of Polytypism and Stacking Sequences in Few-Layer Molybdenum Diselenide by Raman Spectroscopy. *Adv. Mater.* **2015**, *27*, 4502−4508.

(32) Pan, Y.; Li, S.; Rahaman, M.; Milekhin, I.; Zahn, D. R. T. Signature of lattice dynamics in twisted 2D homo/hetero-bilayers. *2D Mater.* **2022**, *9*, 045018.

(33) Rahman, S.; Sun, X. Q.; Zhu, Y.; Lu, Y. R. Extraordinary phonon dsplacement and giant resonance raman enhancement in WSe_2/WS_2 moiré heterostructures. *ACS Nano* **2022**, *16*, 21505−21517.

(34) Maity, I.; Mostofi, A. A.; Lischner, J. Chiral valley phonons and flat phonon bands in moiré materials. *Phys. Rev. B* **2022**, *105*, L041408.

(35) Wu, X. P.; WanG, X.; Li, H. L.; Zeng, Z. X. S.; Zheng, B. Y.; Zhang, D. L.; Li, F.; Zhu, X. L.; Jiang, Y.; Pan, A. L. Vapor growth of WSe_2/WS_2 heterostructures with stacking dependent optical properties. *Nano Res.* **2019**, *12*, 3123−3128.

(36) Suri, N.; Wang, C.; Zhang, Y. H.; Xiao, D. Chiral phonons in moiré superlattices. *Nano Lett.* **2021**, *21*, 10026−10031.

(37) Krisna, L. P. A.; Koshino, M. Moiré phonons in graphene/hexagonal boron nitride moire superlattice. *Phys. Rev. B* **2023**, *107*, 115301.

(38) Liu, X. Q.; Peng, R.; Sun, Z. R.; Liu, J. P. Moiré phonons in magic-angle twisted bilayer graphene. *Nano Lett.* **2022**, *22*, 7791−7797.

(39) Chen, S. Y.; Zheng, C. X.; Fuhrer, M. S.; Yan, J. Helicity-resolved raman scattering of MoS_2, $MoSe_2$, WS_2, and WSe_2 atomic layers. *Nano Lett.* **2015**, *15*, 2526−2532.

(40) Huang, J. Q.; Liu, Z. Y.; Yang, T.; Zhang, Z. D. New selection rule of resonant Raman scattering in MoS_2 monolayer under circular polarization. *J. Mater. Sci. Technol.* **2022**, *102*, 132−136.

(41) Shan, Y. B.; Yue, X. F.; Chen, J. J.; Ekoya, B. G. M.; Han, J. K.; Hu, L. G.; Liu, R.; Qiu, Z. J.; Cong, C. X. Pristine interlayer coupling for strain engineering of WS_2/WSe_2 nanosheet-based van der Waals heterostructures. *ACS Appl. Nano Mater.* **2022**, *5*, 17986−17994.

(42) Lian, B.; Wang, Z. J.; Bernevig, B. A. Twisted bilayer graphene: A phonon-driven superconductor. *Phys. Rev. Lett.* **2019**, *122*, 257002.

(43) Koshino, M.; Nam, N. N. T. Effective continuum model for relaxed twisted bilayer graphene and moiré electron-phonon interaction. *Phys. Rev. B* **2020**, *101*, 195425.

(44) Eliel, G. S. N.; Moutinho, M. V. O.; Gadelha, A. C.; Righi, A.; Campos, L. C.; Ribeiro, H. B.; Chiu, P. W.; Watanabe, K.; Taniguchi, T.; Puech, P.; et al. Intralayer and interlayer electron-phonon interactions in twisted graphene heterostructures. *Nat. Commun.* **2018**, *9*, 1221.

(45) Jin, C. H.; Kim, J.; Suh, J.; Shi, Z. W.; Chen, B.; Fan, X.; Kam, M.; Watanabe, K.; Taniguchi, T.; Tongay, S.; Zettl, A.; Wu, J. Q.; Wang, F. Interlayer electron-phonon coupling in WSe_2/hBN heterostructures. *Nat. Phys.* **2017**, *13*, 127−131.

(46) Chow, C. M.; Yu, H. Y.; Jones, A. M.; Yan, J. Q.; Mandrus, D. G.; Taniguchi, T.; Watanabe, K.; Yao, W.; Xu, X. D. Unusual exciton-phonon interactions at van der Waals engineered interfaces. *Nano Lett.* **2017**, *17*, 1194−1199.

(47) Wu, K.; Zhong, H. X.; Guo, Q. B.; Tang, J. B.; Zhang, J.; Qian, L. H.; Shi, Z. F.; Zhang, C. D.; Yuan, S. J.; Zhang, S. P.; Xu, H. X. Identification of twist-angle-dependent excitons in WS_2/WSe_2 heterobilayers. *Natl. Sci. Rev.* **2022**, *9*, nwab135.

(48) Cong, C. X.; Shang, J. Z.; Wu, X.; Cao, B. C.; Peimyoo, N.; Qiu, C.; Sun, L. T.; Yu, T. Synthesis and Optical Properties of Large-Area Single-Crystalline 2D Semiconductor WS2Monolayer from Chemical Vapor Deposition. *Adv. Opt. Mater.* **2014**, *2*, 131−136.

(49) Berkdemir, A.; Gutiérrez, H. R.; Botello-Méndez, A. R.; Perea-López, N.; Elías, A. L.; Chia, C. I.; Wang, B.; Crespi, V. H.; López-Urías, F.; Charlier, J. C.; Terrones, H.; Terrones, M. Identification of individual and few layers of WS_2 using Raman Spectroscopy. *Sci. Rep.* **2013**, *3*, 1755.

(50) Zhao, Y. Y.; Luo, X.; Li, H.; Zhang, J.; Araujo, P. T.; Gan, C. K.; Wu, J.; Zhang, H.; Quek, S. Y.; Dresselhaus, M. S.; Xiong, Q. H. Interlayer breathing and shear modes in few-trilayer MoS_2 and WSe_2. *Nano Lett.* **2013**, *13*, 1007−1015.

https://doi.org/10.1021/acsami.4c06488
ACS Appl. Mater. Interfaces 2024, 16, 44186−44192